Journal of Materials Chemistry A

ROYAL SOCIETY OF CHEMISTRY

COMMUNICATION

View Article Online
View Journal | View Issue

Check for updates

Cite this: *J. Mater. Chem. A*, 2024, **12**, 7522

Received 15th January 2024
Accepted 4th March 2024

DOI: 10.1039/d4ta00326h

rsc.li/materials-a

Unveiling the ligand-mediated phase engineering mechanism in two-dimensional transition metal chalcogenides through coordination geometry control†

Sungju Jun, ‡[ac] Joo-Won Lee, ‡[a] Sung-Chul Kim, [b] Soong Ju Oh [c] and Sohee Jeong *[a]

While metastable metallic phases of group-VI transition metal dichalcogenide (TMDC) nanosheets exhibit intriguing and unprecedented characteristics, the development of reliable synthetic methodologies, particularly in direct solution-based synthesis, remains a challenge due to the lack of understanding of molecular leverage of the metal–ligand coordination geometry for obtaining metastable phases in two-dimensional (2D) TMDCs. Here, we describe an effective solution-based approach for directly synthesizing metastable metallic phases by unveiling the criterion for phase-selective formation, using appropriate ligands. Specifically, metallic 1T′-WSe_2 and 1T-WS_2 nanosheets were obtained with trioctylphosphine oxide, whereas 2H-WSe_2 and 2H-WS_2 nanosheets were formed using oleylamine. Spectroscopic analysis, including X-ray pre-edge absorption, revealed that phosphine oxide ligands (–O═P) induce the distorted octahedral metal–ligand geometry, followed by the phase-selective formation of metallic 1T′ and 1T phases. Meanwhile, amine ligands ($-NH_2$), accompanied by the trigonal prismatic metal–ligand geometry, exclusively lead to the production of 2H phases. This strategy was applied using hexadecylamine and triphenylphosphine oxide to produce 2H and 1T′ phases, respectively. As a proof-of-concept study, metallic 1T′-WSe_2 shows enhanced hydrogen evolution activity with long-term durability. This strategy, controlling the metal–ligand coordination geometry by the choice of suitable ligands, offers a new guideline for securing metastable phases in 2D TMDCs.

Interest has surged in 2D layered nanomaterials such as TMDCs because these TMDCs exhibit remarkable catalytic, optical, and electronic properties due to the presence of d-electrons in transition metals distinct from graphene.[1–5] Also, with an emerging direct band gap in the monolayer and diverse electrical properties from semiconducting to metallic,[6,7] TMDCs have found applications in energy harvesting and storage. Notably, semiconducting TMDCs like 2H-MoS_2 and 2H-WS_2 served as photocatalysts,[8,9] while metallic 1T-MoS_2 and 1T-$MoSe_2$ were utilized as electrochemical catalysts.[10,11] Existing synthetic protocols for group-VI TMDCs (MCh_2, M = Mo, W; Ch = S, Se) primarily focused on producing thermodynamically stable 2H-MCh_2 with the trigonal prismatic (TPR-6) coordination geometry of M using conventional methods like chemical vapor deposition and solution-based synthesis.[12–14] Conversely, metastable 1T′-MCh_2 and 1T-MCh_2 with distorted octahedral and octahedral (dOC-6 and OC-6) coordination geometries of M have been obtained through post-treatments on 2H-MCh_2, such as intercalation/exfoliation and chemical treatment.[15–17] These procedures, however, introduce chemical impurities like cations inside of TMDCs, compelling a need for the direct solution-based synthesis of metallic MCh_2 to avoid interference from chemical impurities. While some reports provided colloidal strategies for the fabrication of phase-controlled MCh_2,[18–23] the crucial chemical factor for precise phase engineering, especially into metallic phases with dOC-6 and OC-6 geometries, remains underexplored.

In this study, we present a direct solution-based synthetic approach for obtaining metastable metallic WCh_2 by meticulously manipulating the metal–ligand coordination geometry in W complex molecules with the choice of suitable ligands as a pivotal factor guiding the synthesis towards the selective production of 2H-WCh_2 and 1T′-/1T-WCh_2. According to the theoretical study,[24] metastable phases of WCh_2 are more stable and feasible due to their lower unit lattice energies compared to $MoCh_2$. Therefore, this study focuses on the phase control in WCh_2 as a representative case. X-ray spectroscopic investigation along with X-ray pre-edge absorption reveals that specific functional groups ($-NH_2$ and –O═P) in the amine ligands (OLAm and HDAm, standing for oleylamine and

[a]*Materials Architecturing Research Center, Korea Institute of Science and Technology, 5, Hwarang-ro 14 gil, Seongbuk-gu, Seoul, 02792, South Korea. E-mail: soheejeong@kist.re.kr*

[b]*Advanced Analysis and Data Center, Korea Institute of Science and Technology, 5, Hwarang-ro 14 gil, Seongbuk-gu, Seoul, 02792, South Korea*

[c]*Department of Materials Science and Engineering, Korea University, 145 Anam-ro, Seongbuk-gu, Seoul, 02841, South Korea*

† Electronic supplementary information (ESI) available. See DOI: https://doi.org/10.1039/d4ta00326h

‡ S. Jun and J.-W. Lee contributed equally.

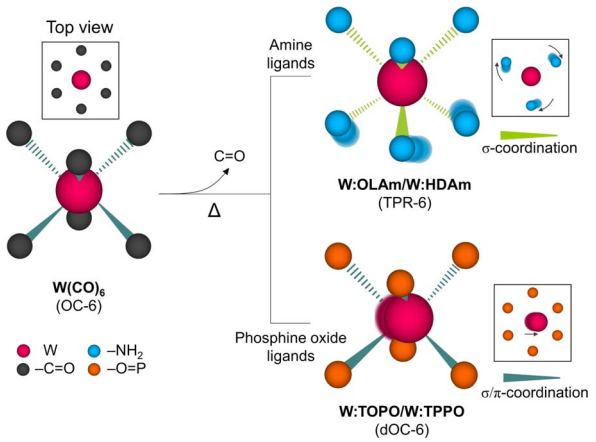

Scheme 1 Illustration showing the control of metal–ligand coordination geometry in W complex molecules by using the amine ligands and phosphine oxide ligands.

hexadecylamine) and phosphine oxide ligands (TOPO and TPPO, abbreviations for trioctylphosphine oxide and triphenylphosphine oxide) drive into W complex molecules with the TPR-6 geometry (W : OLAm and W : HDAm) and the dOC-6 geometry (W : TOPO and W : TPPO), respectively, as shown in Scheme 1. In addition, Raman analysis bridges the gap between the control of metal–ligand coordination geometry and the phase-selective formation of 2H-WCh_2 and 1T′-/1T-WCh_2. As a test for electrocatalytic applications, 1T′-WSe_2 proves the improved hydrogen evolution reaction (HER) performance regarding overpotential, Tafel slope, and durability. While ligands have been extensively studied in 2D layered nanomaterial synthesis, the role of metal–ligand coordination geometry in phase control has been overlooked. To the best of our knowledge, this is the first attempt to demonstrate that the metal–ligand coordination geometry at the molecular level significantly influences the phase engineering of 2D TMDCs, which even facilitates the formation of metastable phases.

We first conducted the synthesis of WSe_2 nanosheets by reacting $W(CO)_6$ and Se in the presence of OLAm and TOPO as a representative of amine ligands and phosphine oxide ligands, affording 2H-WSe_2 and 1T′-WSe_2, respectively. For WSe_2 nanosheets synthesized with OLAm (2H-WSe_2 : OLAm), W hexagonal arrays which correspond to the atomic configuration of the 2H phase with the TPR-6 coordination were observed (Fig. 1a, b and e) by high-angle annular dark-field scanning transmission electron microscopy (HAADF-STEM) imaging. In contrast, when the TOPO ligand was utilized instead of OLAm, WSe_2 nanosheets exhibited a clear characteristic atomic arrangement indicative of the metallic 1T′ phase with the dOC-6 coordination (1T′-WSe_2 : TOPO), displaying aligned W zig–zag chains (Fig. 1c–e). Both 2H-WSe_2 : OLAm and 1T′-WSe_2 : TOPO were found to show less than 4 layers in thickness and 10–15 nm in diameter and have an interlayer distance of 0.64 nm based on high-resolution TEM images (Fig. S1 and S2†). The 1T′ phase uniquely features zig–zag chains on the basal plane even when it has multilayers, unlike other polytypes such as T_d and 2M phases.[25–30] Both monolayer and bilayer regions were detected

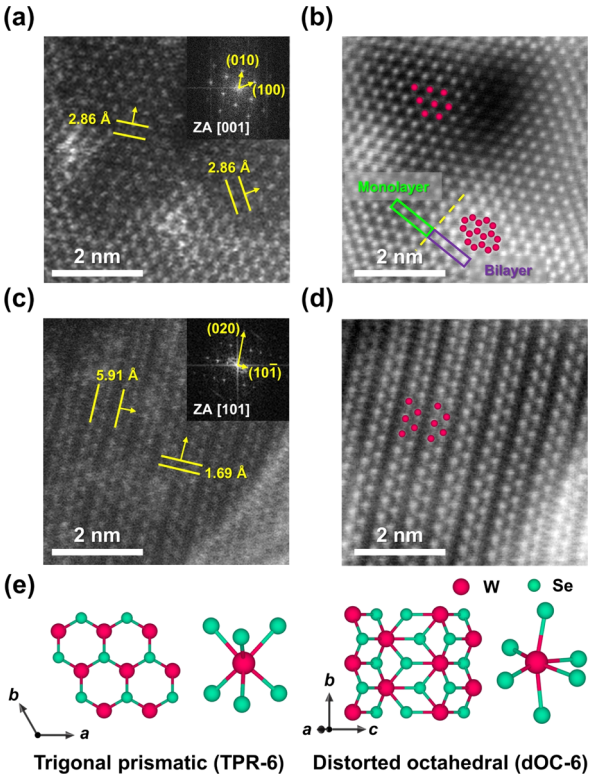

Fig. 1 (a) Top-view HAADF-STEM image and FFT pattern (inset) of 2H-WSe_2 : OLAm. (b) Inverse FFT image of 2H-WSe_2 : OLAm showing W hexagonal arrays. (c) Top-view HAADF-STEM image and FFT pattern (inset) of 1T′-WSe_2 : TOPO. (d) Inverse FFT image of 1T′-WSe_2 : TOPO emphasizing W zig–zag chains. (e) Schematic illustration presenting the top-view atomic arrangement in monolayer and the W coordination geometry of 2H-WSe_2 and 1T′-WSe_2.

in 2H-WSe_2 : OLAm from the intensity profile (Fig. S3†). The fast Fourier transform (FFT) analysis of WSe_2 nanosheets confirmed d-spacings along the basal planes of 2H-WSe_2 : OLAm ($d_{100} = d_{010} = 2.86$ Å) and 1T′-WSe_2 : TOPO ($d_{10-1} = 5.91$ Å and $d_{020} = 1.69$ Å).[31,32]

To further investigate the distinguishing features of both WSe_2 nanosheets, powder X-ray diffraction (PXRD), Raman spectroscopy, and X-ray photoelectron spectroscopy (XPS) were employed. In Fig. 2a, the PXRD patterns of 2H-WSe_2 : OLAm and 1T′-WSe_2 : TOPO closely match with the reported crystallographic structures.[31,32] Specifically, the diffraction peaks corresponding to (100) and (103) planes in 2H-WSe_2 : OLAm indicate the regular interval of W atoms, while the (40−2) diffraction peak in 1T′-WSe_2 : TOPO reflects the Peierls distortion (Fig. S4†).[33] From the Raman measurements which specialize in distinguishing the phase of TMDCs, 2H-WSe_2 : OLAm showed typical vibration modes of E^1_{2g} and A_{1g}, while 1T′-WSe_2 : TOPO exhibited three peaks with low intensities at 217, 236, and 257 cm^{-1} (Fig. 2b). This tripartite splitting aligns with recent studies on the phonon dispersion relationships of 1T′-WSe_2.[23,32,34] XPS analysis ascertained differences in binding energy between 2H-WSe_2 : OLAm and 1T′-WSe_2 : TOPO. As shown in Fig. S5,† 1T′-WSe_2 : TOPO exhibits lower binding energies in W 4f and Se 3d levels compared to those of 2H-

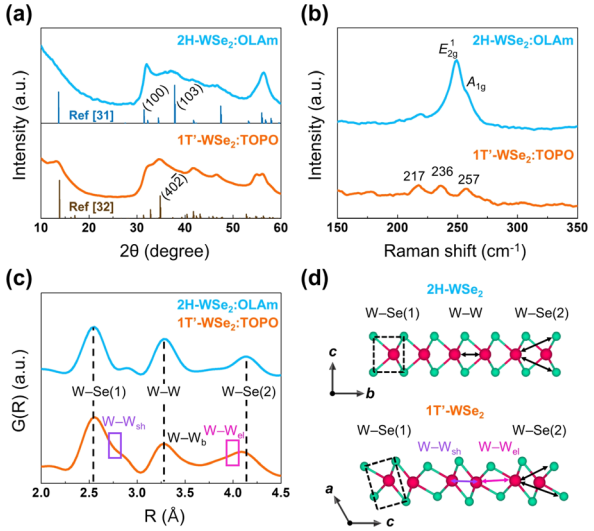

Fig. 2 (a) PXRD results with standard patterns, (b) Raman spectra, and (c) XPDF curves of 2H-WSe_2 : OLAm and 1T′-WSe_2 : TOPO. (d) Side-view representations of 2H-WSe_2 and 1T′-WSe_2.

WSe_2 : OLAm, indicating the redistribution of d-electrons due to the dOC-6 coordination in 1T′-WSe_2 : TOPO.[35] Additionally, both 2H-WSe_2 : OLAm and 1T′-WSe_2 : TOPO presented minor W^{6+} signals attributed to oxidized W edge sites in nanosheets.[23] Nevertheless, 1T′-WSe_2 : TOPO nanosheets with few layers exhibited the structural persistence of the metastable phase (Fig. S6†) even when stored under ambient conditions for up to 60 days at least.

We exploited X-ray atomic pair distribution function (XPDF) analysis to discover structural differences at the atomic scale. Theoretical atomic-pair distances of 2H-WSe_2 and 1T′-WSe_2 are listed in Table S1.†. To start with the nearest W–Se pair, denoted as W–Se(1) in Fig. 2d, the average distances in 2H-WSe_2 : OLAm and 1T′-WSe_2 : TOPO ($D_{W-Se(1)/2H}$ and $D_{W-Se(1)/1T'}$) are marked as 2.54 and 2.58 Å in Fig. 2c, respectively. The dOC-6 coordination of W in 1T′-WSe_2 : TOPO (see Fig. 1e and Table S1†) is expected to correlate with the elongation of W–Se(1) average distance (2.58 Å). Also, arising from the Peierls distortion in the dOC-6 structure, 1T′-WSe_2 : TOPO revealed three distinct types of W–W pairs in the measured range:[22,32,36] one is W–W in the *b*-direction (W–W_b, see Fig. 1e) and the others are referred to as shortened (W–W_{sh}) and elongated (W–W_{el}) pairs (Fig. 2d). These structural features were clearly confirmed, as observed in the purple box ($D_{W-Wsh/1T'} = 2.79$ Å) and pink box ($D_{W-Wel/1T'} = 4.03$ Å) in Fig. 2c. In contrast, 2H-WSe_2 : OLAm exhibits only one type of W–W pair ($D_{W-W/2H} = 3.28$ Å). The peak of W–Se(2) in 1T′-WSe_2 : TOPO is relatively broadened compared to that in 2H-WSe_2 : OLAm, attributed to the dOC-6 coordination of W again.

The ligand-mediated phase engineering syntheses of 2H-WSe_2 and 1T′-WSe_2 were further validated by using alternative amine (HDAm) and phosphine oxide (TPPO). PXRD and Raman results clearly verified the identical phase-selective formation into 2H-WSe_2 : HDAm and 1T′-WSe_2 : TPPO (Fig. S7–S10†). The ligands are pivotal in influencing the phase of WSe_2 nanosheets, as observed in the experiments. This phenomenon can be examined by the difference in the ligand-mediated coordination geometry of W complex molecules, which determines the resultant crystal structure grown in solution.[37] Thus, we systematically investigated the W precursor complexes ($W(CO)_6$: OLAm and $W(CO)_6$: TOPO, obtained from the reaction of $W(CO)_6$ and each ligand only) to identify the underlying phase engineering mechanism of WSe_2 nanosheets by Fourier-transform infrared (FTIR), Raman, and XPS spectroscopic analyses. A decrease in IR active C=O stretching signals with increasing temperature was observed in both $W(CO)_6$: OLAm and $W(CO)_6$: TOPO, ultimately leading to the absence of C=O stretching signals (Fig. 3a). The C=O stretching signals of $W(CO)_6$: OLAm and $W(CO)_6$: TOPO at 50 °C are comparable to those of pristine $W(CO)_6$ (Fig. S11†). However, the C=O signals nearly disappear above 150 °C, implying the formation of W : OLAm and W : TOPO (see next), as depicted in Scheme 1.

In Fig. 3b, Raman spectra of $W(CO)_6$: OLAm-200 and $W(CO)_6$: TOPO-200, obtained at 200 °C, exhibit distinct vibrational modes corresponding to the coordination environments of W. Notably, Raman peaks of W–N (808.1 cm^{-1}) and W–O (707.7 and 946.5 cm^{-1}), analogous to six-coordinate W compounds such as WN[38,39] and WO_3,[40] were measured in $W(CO)_6$: OLAm-200 and $W(CO)_6$: TOPO-200, respectively. Unlike WO_3, the vibration mode implying a bulk network structure (805 cm^{-1}) was not detected in the spectrum of $W(CO)_6$: TOPO-200, but the terminal W=O signal was noticeable, indicating the molecular structure of $W(CO)_6$: TOPO-200.[40] The W 4f XPS spectrum of $W(CO)_6$: OLAm-200 (Fig. S12†) in connection with the Raman result implies W^{6-} species (37.1 and 35.0 eV)[41] by forming W–NH_2 bonds. Similarly, the spectrum of $W(CO)_6$: TOPO-200 exhibits W^{6+} doublet peaks (37.5 and 35.6 eV) contributed by W–O=P bonds. The broadened spectral feature in $W(CO)_6$: TOPO-200 attributed to the peak indicating a lower valence (34.0 eV) can be assigned to a slightly lower coordination number by TOPO (<6) compared to the $W(CO)_6$: OLAm-200 due to its relatively weak affinity with W and bulkiness.[42] In summary, $W(CO)_6$ undergoes the removal of C=O and the formation of W–NH_2 and W–O=P bonds in the presence of OLAm and TOPO, respectively.

To directly understand the change in metal–ligand coordination geometry of $W(CO)_6$: OLAm and $W(CO)_6$: TOPO, we performed pre-edge analysis at the W L_1-edge region using X-ray absorption near edge structure (XANES) measurements. According to a selection rule and p–d hybridization (Fig. S13†),[43,44] pristine $W(CO)_6$ with the OC-6 metal–ligand geometry showed no pre-edge features (Fig. S14†). In contrast, both $W(CO)_6$: OLAm-150 (reacted at 150 °C) and $W(CO)_6$: OLAm-200 exhibited prominent pre-edge peaks at ~12 102 eV (Fig. 3c), strongly indicating the existence of TPR-6 metal–ligand geometry (Fig. S13†). For $W(CO)_6$: OLAm-100 (reacting at 100 °C), only a rising-edge curve was observed, suggesting the retention of the OC-6 metal–ligand geometry and W–C=O bonds from $W(CO)_6$,[18] in agreement with FTIR results. Interestingly, minimal pre-edge absorption was observed in all $W(CO)_6$: TOPO samples (Fig. 3d), verifying the dOC-6 metal–ligand geometry.[44] A similar pattern of pre-edge absorption was detected in XANES spectra of $W(CO)_6$: HDAm-200 (Fig. S15†)

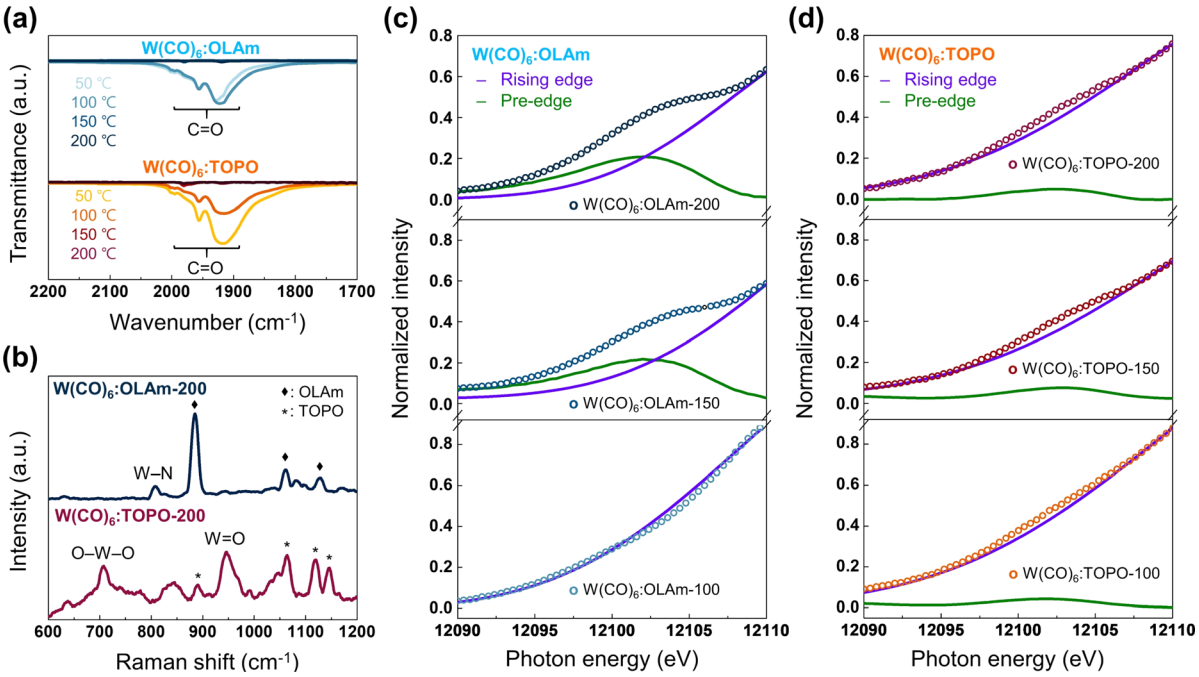

Fig. 3 (a) FTIR transmittance spectra of $W(CO)_6$: OLAm and $W(CO)_6$: TOPO obtained at various reaction temperatures. (b) Raman spectra of $W(CO)_6$: OLAm-200 and $W(CO)_6$: TOPO-200. Curve fitting of W L_1-edge XANES spectra of (c) $W(CO)_6$: OLAm-T and (d) $W(CO)_6$: TOPO-T, where $T = 100$, 150, and 200, respectively.

and $W(CO)_6$: TPPO-200 (Fig. S16†), which shows that an identical W-ligand coordination geometry was produced using the same type of ligands. These XANES results confirmed that amine ligands (OLAm and HDAm) and phosphine oxide ligands (TOPO and TPPO) are capable of manipulating the metal–ligand geometry in W complex molecules into the TPR-6 and the dOC-6 geometry, respectively.

According to the criterion for the metal–ligand coordination geometry of six-coordinate W complexes, the OC-6 coordination is dominant except for the condition of a high-valence W and exclusive σ-coordination between W and ligands.[45] $W(CO)_6$: OLAm-200 with the oxidation state of +6 is expected to form σ-coordination bonds between W and $-NH_2$ functional groups, referring to previous studies on W–NH_2 complexes about bonding parameters,[46] molecular geometries (Fig. S17†),[47] and coordination reaction.[48] Thus, it was revealed that $W(CO)_6$: OLAm-200 and $W(CO)_6$: HDAm-200 show the TPR-6 metal–ligand geometry. In contrast, $W(CO)_6$: TOPO samples maintain the $W(CO)_6$ geometry in the form of dOC-6 (Fig. 3d) due to σ/π-coordination bonds between W and –O═P. The π-coordination between W and –O═P is highly attributed to molecular π bonds between O and P in phosphine oxide ligands.[46,49] In this context, *ex situ* Raman measurements in Fig. 4 completely concluded the effect of controlling the metal–ligand coordination geometry on the phase engineering of WSe_2 nanosheets. The additional selenization process for 60 min converted $W(CO)_6$: OLAm-200 and $W(CO)_6$: TOPO-200 into 2H-WSe_2 and 1T′-WSe_2 nanosheets, respectively, conserving each coordination geometry of W.

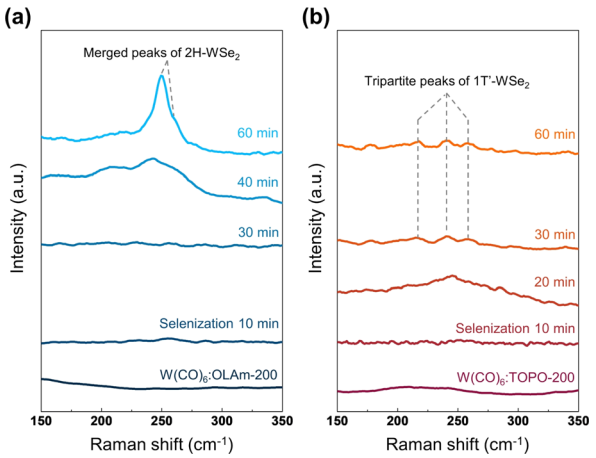

Fig. 4 Raman spectra of (a) $W(CO)_6$: OLAm-200 and (b) $W(CO)_6$: TOPO-200, treated by the selenization process from 10 min to 60 min.

Our phase engineering mechanism was also applicable for synthesizing WS_2 nanosheets. The resulting products grown with each OLAm and TOPO (2H-WS_2 : OLAm and 1T-WS_2 : TOPO) were verified to show the atomic configurations of 2H and 1T phases (Fig. S18a–d†), which agrees with the previously reported structures (Fig. S18e†).[50,51] PXRD patterns confirmed a slight shift of the (100) diffraction peak in 1T-WS_2 : TOPO compared to the 2H-WS_2 : OLAm (Fig. S19†), reflecting a slight expansion of the (100) *d*-spacing in 1T-WS_2.[52]

As a proof-of-concept application study, semiconducting and metallic WCh_2 nanosheets were utilized as HER electrocatalysts. In Fig. 5a–c, 1T′-WSe_2 : TOPO exhibited lower overpotential at -10 mA cm^{-2} (0.21 V), lower Tafel slope (115 mV dec^{-1}), and higher double-layer capacitance (18.21 mF cm^{-2}) compared to those of 2H-WSe_2 : OLAm. Double-layer

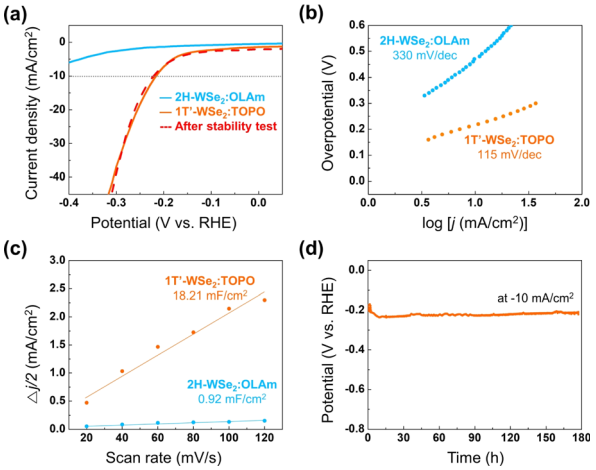

Fig. 5 (a) Polarization curves, (b) Tafel slopes, and (c) double-layer capacitances of 2H-WSe_2 : OLAm and 1T′-WSe_2 : TOPO. (d) Long-term durability of 1T′-WSe_2 : TOPO.

capacitances were obtained by sequential cyclic voltammetry measurements with varying scan rates (Fig. S20†). Also, in Fig. S21,† 1T-WS_2 : TOPO showed lower overpotential (0.37 V) compared to the 2H-WS_2 : OLAm (0.68 V). Notably, 1T′-WSe_2 : TOPO proved long-term durability for 180 h (Fig. 5d) and still showed an identical polarization curve even after the stability test (Fig. 5a). This can be attributed to the conserved metallic phase and nanosheet morphology of the 1T′-WSe_2 : TOPO catalyst (Fig. S22 and S23†). Also, the structural persistence of 1T′-WSe_2 : TOPO was further confirmed by measuring polarization curves of samples stored under ambient conditions for seven days (1T-WSe_2-7 days) and 60 days (1T′-WSe_2-60 days), as shown in Fig. S24.† Accordingly, the HER performance of 1T′-WSe_2 : TOPO is comparable to that of other WCh_2 catalysts (Table S2†). Thus, we found the possibility of phase-engineered WSe_2 nanosheets for practical electrocatalytic applications.

In conclusion, our investigation has revealed that achieving the phase-controlled WCh_2 by a direct solution-phase synthesis necessitates the modulation of metal–ligand coordination geometry in W complex molecules through the use of appropriate ligands. Various spectroscopic analyses confirmed that phosphine oxide ligands, which form σ/π-coordination with W through an –O═P functional group, can exclusively induce the formation of metastable metallic WCh_2. This process proceeds from W : TOPO and W : TPPO with the dOC-6 metal–ligand coordination geometry. Otherwise, amine ligands lead to the formation of 2H phases of WCh_2. The phase-engineered 1T′-WSe_2 nanosheets show promising HER performance in activity and durability. Therefore, once suitable ligands facilitating selective geometry formation are found, our approach holds significant potential for synthesizing and exploring various metastable phases in 2D TMDCs.

Author contributions

S. Jun and J.-W. Lee contributed equally to this work. S. Jun and J.-W. Lee synthesized WSe_2 and WS_2, conducted XRD and Raman measurements, carried out TEM and XANES, analysed HER measurement results and discussed about the raw data. S.-C. Kim conducted XPDF measurements and helped with the discussion of the results. S. J. Oh contributed suggestions on the synthesis. S. Jeong supervised the work.

Conflicts of interest

There are no conflicts to declare.

Acknowledgements

This research was supported by the National R&D Program (NRF-2020M3H4A3106354) and the program of Future Hydrogen Original Technology Development (NRF-2021M3I3A1083946) through the National Research Foundation of Korea (NRF) funded by the Korean government (Ministry of Science and ICT (MSIT)), Basic Science Research Program through the National Research Foundation of Korea (NRF) funded by the Ministry of Education (NRF-2021R1A6A3A01087461), and the Future Key Technology Program (Project No. 2E32511) funded by the Korea Institute of Science and Technology.

References

1 K. S. Novoselov, A. K. Geim, S. V. Morozov, D. Jiang, Y. Zhang, S. V. Dubonos, I. V. Grigorieva and A. A. Firsov, *Science*, 2004, **306**, 666–669.
2 Y. Zhang, L. Zhang and C. Zhou, *Acc. Chem. Res.*, 2013, **46**, 2329–2339.
3 H. Li, C. Tsai, A. L. Koh, L. Cai, A. W. Contryman, A. H. Fragapane, J. Zhao, H. S. Han, H. C. Manoharan, F. Abild-Pedersen, J. K. Norskov and X. Zheng, *Nat. Mater.*, 2016, **15**, 48–53.
4 C. Lattyak, M. Vehse, M. A. Gonzalez, D. Pareek, L. Gütay, S. Schäfer and C. Agert, *Adv. Opt. Mater.*, 2022, **10**, 2102226.
5 R. Kappera, D. Voiry, S. E. Yalcin, B. Branch, G. Gupta, A. D. Mohite and M. Chhowalla, *Nat. Mater.*, 2014, **13**, 1128–1134.
6 S. Krishnamurthi and G. Brocks, *NPJ 2D Mater. Appl.*, 2021, **5**, 43.
7 S. Chowdhury, P. Venkateswaran and D. Somvanshi, *Phys. B: Condens.*, 2023, **653**, 414668.
8 A. Rahman, J. R. Jennings, A. L. Tan and M. M. Khan, *ACS Omega*, 2022, **7**, 22089–22110.
9 P. Xiao, J. Lou, H. Zhang, W. Song, X.-L. Wu, H. Lin, J. Chen, S. Liu and X. Wang, *Catal. Sci. Technol.*, 2018, **8**, 201–209.
10 Z. Zhu, A. Mosallanezhad, D. Sun, X. Lei, X. Liu, Z. Pei, G. Wang and Y. Qian, *Energy Fuels*, 2021, **35**, 5613–5626.
11 Q. Xia, L. Zhao, D. Li, J. Wang, L. Liu, C. Hou, X. Liu, H. Xu, F. Dang and J. Zhang, *J. Mater. Chem. A*, 2021, **9**, 19922–19931.
12 B. Kalanyan, W. A. Kimes, R. Beams, S. J. Stranick, E. Garratt, I. Kalish, A. V. Davydov, R. K. Kanjolia and J. E. Maslar, *Chem. Mater.*, 2017, **29**, 6279–6288.

13 R. Konar, Rosy, I. Perelshtein, E. Teblum, M. Telkhozhayeva, M. Tkachev, J. J. Richter, E. Cattaruzza, A. Pietropolli Charmet, P. Stoppa, M. Noked and G. D. Nessim, *ACS Omega*, 2020, **5**, 19409–19421.
14 A. Midya, A. Ghorai, S. Mukherjee, R. Maiti and S. K. Ray, *J. Mater. Chem. A*, 2016, **4**, 4534–4543.
15 K. Leng, Z. Chen, X. Zhao, W. Tang, B. Tian, C. T. Nai, W. Zhou and K. P. Loh, *ACS Nano*, 2016, **10**, 9208–9215.
16 E. Er, H.-L. Hou, A. Criado, J. Langer, M. Möller, N. Erk, L. M. Liz-Marzán and M. Prato, *Chem. Mater.*, 2019, **31**, 5725–5734.
17 Y. Ma, B. Liu, A. Zhang, L. Chen, M. Fathi, C. Shen, A. N. Abbas, M. Ge, M. Mecklenburg and C. Zhou, *ACS Nano*, 2015, **9**, 7383–7391.
18 P. Zhou, P. Schiettecatte, M. Vandichel, A. Rousaki, P. Vandenabeele, Z. Hens and S. Singh, *Cryst. Growth Des.*, 2021, **21**, 1451–1460.
19 J. Q. Geisenhoff, A. K. Tamura and A. M. Schimpf, *Chem. Commun.*, 2019, **55**, 8856–8859.
20 B. Mahler, V. Hoepfner, K. Liao and G. A. Ozin, *J. Am. Chem. Soc.*, 2014, **136**, 14121–14127.
21 Z. Liu, K. Nie, X. Qu, X. Li, B. Li, Y. Yuan, S. Chong, P. Liu, Y. Li, Z. Yin and W. Huang, *J. Am. Chem. Soc.*, 2022, **144**, 4863–4873.
22 M. S. Sokolikova, P. C. Sherrell, P. Palczynski, V. L. Bemmer and C. Mattevi, *Nat. Commun.*, 2019, **10**, 712.
23 A. Niebur, A. Söll, P. Haizmann, O. Strolka, D. Rudolph, K. Tran, F. Renz, A. P. Frauendorf, J. Hübner, H. Peisert, M. Scheele and J. Lauth, *Nanoscale*, 2023, **15**, 5679–5688.
24 K.-A. N. Duerloo, Y. Li and E. J. Reed, *Nat. Commun.*, 2014, **5**, 4214.
25 T. Lu, Y. Wang, G. Cai, H. Jia, X. Liu, C. Zhang, S. Meng and M. Liu, *Mater. Futures*, 2023, **2**, 015001.
26 Y. M. Itahashi, Y. Nohara, T. Ideue, T. Akiba, H. Takahashi, S. Ishiwata and Y. Iwasa, *Phys. Rev. Res.*, 2023, **5**, L022022.
27 R. Konar, B. Rajeswaran, A. Paul, E. Teblum, H. Aviv, I. Perelshtein, I. Grinberg, Y. R. Tischler and G. D. Nessim, *ACS Omega*, 2022, **7**, 4121–4134.
28 J. Y. Kim, I. H. Kwak, I. S. Kwon, Q. A. Sial, J. Ihsan, G. M. Zewdie, J. Park and H. S. Kang, *J. Mater. Chem. A*, 2023, **11**, 19619–19628.
29 X. Guo, T. Wu, S. Zhao, Y. Fang, S. Xu, M. Xie and F. Huang, *ACS Appl. Energy Mater.*, 2022, **5**, 7674–7680.
30 H. Paudyal and E. R. Margine, *J. Mater. Chem. C*, 2022, **10**, 7917–7924.
31 W. Schutte, J. De Boer and F. Jellinek, *J. Solid State Chem.*, 1987, **70**, 207–209.
32 Z. Lai, Q. He, T. H. Tran, D. V. M. Repaka, D. D. Zhou, Y. Sun, S. Xi, Y. Li, A. Chaturvedi, C. Tan, B. Chen, G. H. Nam, B. Li, C. Ling, W. Zhai, Z. Shi, D. Hu, V. Sharma, Z. Hu, Y. Chen, Z. Zhang, Y. Yu, X. Renshaw Wang, R. V. Ramanujan, Y. Ma, K. Hippalgaonkar and H. Zhang, *Nat. Mater.*, 2021, **20**, 1113–1120.
33 D. H. Keum, S. Cho, J. H. Kim, D.-H. Choe, H.-J. Sung, M. Kan, H. Kang, J.-Y. Hwang, S. W. Kim, H. Yang, K. J. Chang and Y. H. Lee, *Nat. Phys.*, 2015, **11**, 482–486.
34 W. Chen, X. Xie, J. Zong, T. Chen, D. Lin, F. Yu, S. Jin, L. Zhou, J. Zou, J. Sun, X. Xi and Y. Zhang, *Sci. Rep.*, 2019, **9**, 2685.
35 W. Zhao, J. Pan, Y. Fang, X. Che, D. Wang, K. Bu and F. Huang, *Chem.–Eur. J.*, 2018, **24**, 15942–15954.
36 J. W. González, E. Flórez and J. D. Correa, *J. Mol. Liq.*, 2024, **396**, 123904.
37 D. P. Dinega and M. G. Bawendi, *Angew. Chem., Int. Ed.*, 1999, **38**, 1788–1791.
38 C. Pardanaud, D. Dellasega, M. Passoni, C. Martin, P. Roubin, Y. Addab, C. Arnas, L. Couëdel, M. Minissale, E. Salomon, G. Giacometti, A. Merlen, E. Bernard, R. Mateus, E. Alves, Z. Siketic, I. B. Radovic and A. Hakola, *Nucl. Fusion*, 2020, **60**, 086004.
39 P. Shen, X. Li, Y. Luo, Y. Guo, X. Zhao and K. Chu, *ACS Nano*, 2022, **16**, 7915–7925.
40 B. Pecquenard, H. Lecacheux, J. Livage and C. Julien, *J. Solid State Chem.*, 1998, **135**, 159–168.
41 S. Nomoto, H. Kitamura, S. Takase and Y. Shimizu, *Electrochemistry*, 2022, **90**, 087005.
42 J. Q. Geisenhoff, H. Yin, N. Oget, H. Chang, L. Chen and A. M. Schimpf, *Front. Nanotechnol.*, 2022, **4**, 1026635.
43 U. Jayarathne, P. Chandrasekaran, A. F. Greene, J. T. Mague, S. DeBeer, K. M. Lancaster, S. Sproules and J. P. Donahue, *Inorg. Chem.*, 2014, **53**, 8230–8241.
44 S. Yamazoe, Y. Hitomi, T. Shishido and T. Tanaka, *J. Phys. Chem. C*, 2008, **112**, 6869–6879.
45 K. Seppelt, *Acc. Chem. Res.*, 2003, **36**, 147–153.
46 R. Brown and G. Dobson, *Inorg. Chim. Acta*, 1972, **6**, 65–71.
47 M. Kaupp, *J. Am. Chem. Soc.*, 1996, **118**, 3018–3024.
48 S. Baskaran, P. Balu and C. Sivasankar, *J. Chem. Sci.*, 2015, **127**, 83–94.
49 D. G. Gilheany, *Chem. Rev.*, 1994, **94**, 1339–1374.
50 B. F. Mentzen and M. Sienko, *Inorg. Chem.*, 1976, **15**, 2198–2202.
51 N. Lee, I. Y. Choi, K.-Y. Doh, J. Kim, H. Sim, D. Lee, S.-Y. Choi and J. K. Kim, *J. Mater. Chem. A*, 2019, **7**, 26378–26384.
52 M. Srinivaas, C.-Y. Wu, J.-G. Duh and J. M. Wu, *ACS Sustainable Chem. Eng.*, 2019, **7**, 10363–10370.